A Co-Doped MnO2 catalyst for Li-CO2 batteries with low overpotential and ultrahigh cyclability.

GE, B., SUN, Y., GUO, J., YAN, X., FERNANDEZ, C., PENG, Q.

2019

WILEY-VCH

DOI: 10.1002/ ((please add manuscript number))
Article type: Full Paper

A Co-Doped MnO_2 Catalyst for Li-CO_2 Batteries with Low Overpotential and Ultrahigh Cyclability

*Bingcheng Ge, Yong Sun, Jianxin Guo, Carlos Fernandez and Qiuming Peng**

Dr. Bingcheng Ge, Yong Sun, Prof. Qiuming Peng
State Key Laboratory of Metastable Materials Science and Technology, Yanshan University, Qinhuangdao 066004, China
E-mail: pengqiuming@gmail.com

Dr. Jianxin Guo
Hebei Provincial Key Lab of Optoelectronic Information Materials, College of Physics Science and Technology, Hebei University, Baoding, 071002, China.

Carlos Fernandez
School of Pharmacy and life sciences, Rober Gordon University, Aberdeen, AB107GJ, United Kingdom

Abstract

Lithium-CO_2 batteries not only capture carbon dioxide to solve the greenhouse effect, but also serve as clean and next-generation energy storage devices on the merits of economical, environmentally-friendly and sustainable aspects. However, the Li-CO_2 batteries are suffering from two main drawbacks: high overpotential and poor cyclability, severely postponing the rhythm of their applications. Herein, we have prepared a new Co-doped alpha-MnO_2 nanowire catalyst for rechargeable Li-CO_2 batteries, which exhibits a high capacity (8160 mA h g^{-1} at a current density of 100 mA g^{-1}), a low overpotential (~0.73 V) and an ultrahigh cyclability (over 500 cycles at a current density of 100 mA g^{-1}), exceeding those of Li-CO_2 batteries reported so far. The reaction mechanisms are interpreted depending on the *in-situ* experimental observations in combination with density functional theory calculations. The outstanding electrochemical properties are mostly associated with a high conductivity, a large fraction of hierarchical channels and a unique Co interstitial doping, which might be of benefit for the diffusion of CO_2, the decomposition of Li_2CO_3 discharge product, and the prohibitions of side reactions between electrolyte and electrode. Consequently, these results shed light on both CO_2 fixation and new Li-CO_2 batteries for energy storage.

Keywords: Lithium-air battery; Catalyst; Low overpotential; Cyclability

1. Introduction

Li-ion batteries have dominated the portable electronics market and revolutionized our daily activities in the past decades.[1] However, these traditional Li-ion batteries can not meet the requirements of high energy density for portable electronic devices and electric vehicles due to their low capacity densities.[2-4] Therefore, the development of a new metal-gas battery with high specific energy density and good cycle stability is believed as a promising strategy to solve this issue. For example, Li-CO_2 battery which has been developed on the basis of Li-O_2 battery has recently attracted attention. This battery system not only bestows a high energy density in terms of electrochemical energy storage, but also alleviates the greenhouse effect by capturing CO_2.[5]

More recently, Li-CO_2 batteries have been attempted as new energy carriers to store renewable energy, in which Li_2CO_3 is the discharge product as indicated as follows: $4Li + 3CO_2 + 4e^- \leftrightarrow 2Li_2CO_3 + C$ (E^0 = 2.80 V *vs*. Li/Li).[6-8] Unfortunately, this incipient prototype battery can only run about 10 cycles. The main reasons are related to two features. Firstly, the insert decomposition of Li_2CO_3 discharge product is prone to adhere on the cathode surface, and then remarkably reduces the capacity.[8] Secondly, the aggregation of Li_2CO_3 product can block the channels of gas diffusion and reduce the conductivity of electrode, resulting in a very high charge potential (>4.3 V).[6] In this regard, an efficient cathode which could provide a high surface area and promote the decomposition of the Li_2CO_3 discharge product is desirable to achieve the high performance of the Li-CO_2 batteries.[9]

Akin to the development of the Li-O_2 batteries, there are two approaches to design effective cathodes. On the one hand, the direct modification and optimization of cathode structures have been regarded as a simple method to improve the properties of the Li-CO_2 batteries. For instance, Zhou *et al.* [10, 11] successfully examine graphene and carbon nanotubes (CNTs) as the cathodes, in which the Li-CO_2 batteries operate for 20

cycles with an overpotential of 1.78 V at 50 mA g^{-1} under a limitative capacity of 1000 mAh g^{-1}. Dai *et al.* [12] devise two kinds of graphene-based materials with defective structures for Li-CO_2 batteries-holey graphene and B,N-co-doped holey graphene, which shows a cycling lifetime over 200 cycles at 1 A g^{-1}, but suffer from a large overpotential (about 1.8 V at 1 A g^{-1}). Liu *et al.*[13] first introduce CNT decorated with RuO_2 as cathode materials for Li-CO_2 batteries, which can deliver high specific capacity together with a lower overpotential.

On the other hand, the development of new catalysts is another effective method to enhance the electrochemical properties of Li-CO_2 batteries. For example, the cobalt–titanium layered oxide-RuO_2 composite with a low over-potential of 0.6 V has been achieved recently.[14] The nanocomposite of anatase titania nanoparticles (TiO_2-NPs) has been established as a high efficient catalyst for the Li-CO_2 battery with favorable cycle performance.[15] The porous Mn_2O_3 catalyst for the Li-CO_2 battery exhibits a durable cyclability for 2000 h (about 50 cycles) at 50 mA g^{-1} and an overpotential of 1.4 V, due to a highly porous structure and an excellent catalytic activity.[16] The cathode which comprising manganese metal-organic frameworks delivers a high discharge specific capacity of 18022 mA h g^{-1} at 50 mA g^{-1}, while still undergoes a high overpotential (>1.2 V).[17] Although enormous progress has been made, achieving a highly cycled Li-CO_2 battery with a low overpotential still remains challenging.

In this work, we have prepared a new Co-doped alpha-MnO_2 nanofiber catalyst, which was effective to improve the electrochemical properties of the Li-CO_2 batteries by increasing the conductivity, enhancing the catalytic activity and prohibiting the side reactions. The Li-CO_2 battery with the optimized Co-doped alpha-MnO_2 nanofiber electrode shows a large capacity of 8160 mA h g^{-1}, a low overpotential of ~0.73 V and an ultrahigh cyclability (500 cycles). The catalyst is highlighted by its simplicity and

high-yield production of a well-defined morphology, which is attributed for the industrial development of Li-CO_2 batteries.

2. Results and discussion

2.1. Electrode characteristics

An electrode with a Co-doped alpha-MnO_2 compound supported by a piece of carbon cloth (CC) was prepared by a simple hydrothermal reaction (the detailed procedure was described in the Experimental Procedure). Specifically, a $KMnO_4$ powder was added to a mixed solution of $MnSO_4 \cdot H_2O$ and $Co(NO_3)_2 \cdot 6H_2O$, and then a CC was immersed in the mixed solution. Subsequently, the reaction mixture was heated in a microwave-assisted reactor at 140 °C for 60 min. Finally, the reacted CC was washed three times with deionized water and dried for 12 hours in a vacuum. The X-ray diffraction (XRD, **Figure. 1a**) patterns shows that a typical (002) peak is detected in the primitive CC sample, which is consistent with our previous result.[18] However, some new peaks are observed after reacting in the single $MnSO_4 \cdot H_2O$ solution. The lattice parameters are a=b=0.98 nm and c=0.28 nm, respectively. They are in agreement with those of pure tetragonal alpha-MnO_2 (JCPDS NO. 44-0141). Comparatively, the similar peaks are also confirmed in the mixed solution of $MnSO_4 \cdot H_2O$ and $Co(NO_3)_2 \cdot 6H_2O$. The intensity of XRD diffraction peaks decreases with the increase of Co-doped content (**Figure. S1**), revealing the crystalline of compounds weaker.

The scanning electron microscopy (SEM, **Figure. 1b-d**) images show that the smooth wires become coarse, and then they are covered by fine nanoscale wires after reacting for 60 min, resulting in the formation of thorn-bush nanofibers. The transmission electron microscopy (TEM, **Figure. 1e**) image reveals that the diameter and length of wires are ~ 50 nm and over 2 μm, respectively. The selected area electron diffraction pattern and high revolution TEM results (**Figure. 1f**) demonstrate that the growth orientation of nanowires is along <001> direction. The planar parameters are 0.32 nm and 0.27 nm, respectively. Both of them are

similar to those of (310) and (001) planes of pure alpha-MnO_2. The low-loss electron energy loss spectroscopy (EELS) profile shows that some new peaks (13.2, 27.2 and 65.7 eV, **Figure. 1g**) are observed in contrast to the primitive alpha-MnO_2 nanowire, indicating the formation of Co-doping alpha-MnO_2 nanowires. Moreover, the Co dopant has also been confirmed by X-ray photoelectron spectroscopy (XPS) analysis (**Figure. 1h**), in which both Mn peaks and Co peaks are involved. The high-resolution XPS spectra of Mn 2*p* (**Figure. 1i**) reveals the concentration of Mn^{4+} (642 eV) and Mn^{3+} (645.0 and 654.0 eV) [19] are 56% and 44%, respectively. The Co-doping increases the amount of Mn^{3+}. Comparatively, Co^{3+}, Co^{2+} and Co^0 are verified in terms of the high resolution Co 2*p* XPS spectra (**Figure. 1j**), wherein the fraction of $Co^{2+}$and Co^{3+} is higher than that of Co^{0+}(below 5%). Therefore, the effect of Co^{0+} on catalytic role has been neglected. The similar multivalent doping has been found in the Co-NiO systems .[20] As a result, this composite cathode which is prepared with the Co^{2+}($Co(NO_3)_2 \cdot 6H_2O$): Mn^{2+} ($MnSO_4 \cdot H_2O$) mole ratio of 0.2:0.8 in the initial solution is mainly composed of Co-containing apha-MnO_2 and CC, and it can be simplified as the $Co_{0.2}Mn_{0.8}O_2$/CC.

To probe the effect of the addition of Co fraction on Co-doped content and microstructure, the molar ratios of Co^{2+}:Mn^{2+} in the initial solutions with a constant total concentration of two ions of 0.1:0.9 and 0.5:0.5 corresponding to $Co_{0.1}Mn_{0.9}O_2$ and $Co_{0.5}Mn_{0.5}O_2$ samples have been investigated. The pure MnO_2 sample is introduced as a reference. The detailed Co concentration in the samples were determined using energy dispersive spectrometer (EDS) (**Table S1**), the elemental content of Co is increased from 0.55 at.% ($Co_{0.1}Mn_{0.9}O_2$) to ~1.12 at.% ($Co_{0.2}Mn_{0.8}O_2$), and it remains stable with further increasing the Co^{2+} concentration. The SEM images (**Figure. S2a-b**) show that the morphologies of Co-doped alpha-MnO_2 samples remain a nanowire structure when the Co-doping fraction is below 0.2. In contrast, the radiating nanowires are severely destroyed and some plate-like precipitates are detected with the Co-doping fraction of 0.5. Note that the same alpha-MnO_2 structure is identified in the

$Co_{0.5}Mn_{0.5}O_2$ sample by HRTEM (**Figure. S2c-e**). This similar trend has also been reported in the Al-doped MnO_2. [21] The energy-dispersive spectrum (EDS) mapping was used to explore the distribution of Co, Mn and O elements in $Co_{0.2}Mn_{0.8}O_2$ nanowires (**Figure S3**), and the results show that Co, Mn and O elements are homogeneously distributed on the nanowires, suggesting that the Co element has uniformly doped into the MnO_2 nanowire, analogous to the data of EDS line scanning (**Figure S3a**).

2.2. Battery performance

The electrochemical properties of the Li-CO_2 batteries with the different cathodes are investigated. The cyclic voltammetry (CV) curves under CO_2 or Ar (**Figure. 2a** and **Figure S4a**) which are measured from 2 to 4.5 V *vs*. Li/Li^+ at a scan rate of 0.2 mV s^{-1} reveal that there are two peaks for the pure alpha-MnO_2/CC cathode, which is totally different from the original CC without reactive peaks. It shows that the oxidation/reduction reactions can take place with the loading of an alpha-MnO_2 catalyst. Attractively, compared with those of the pure alpha-MnO_2/CC cathode, the $Co_{0.2}Mn_{0.8}O_2$/CC cathode exhibits a higher CO_2 reduction reaction onset potential (CO_2RR, ~2.69 V), a lower CO_2 evolution reaction onset potential (CO_2ER, ~3.79 V), and a higher CO_2RR/CO_2ER peak current (~1.04 mA).

Figure. 2b presents the voltage profiles of the Li-CO_2 battery with the $Co_{0.2}Mn_{0.8}O_2$/CC cathode at different current densities. The batteries can yield the capacities of 8203 and 2327 mA h g^{-1} at the current densities of 100 and 500 mA g^{-1} under CO2, respectively. By contrast, the discharge voltages of $Co_{0.2}Mn_{0.8}O_2$/CC cathode were rapidly declined to 2 V without any recognizable plateau under the atmosphere of Ar (**Figure S4b**), indicating that the electrochemical performance did come from the reduction of CO_2. The voltage profiles and long-term cycling performance of the Li-CO_2 batteries with the $Co_{0.2}Mn_{0.8}O_2$/CC and MnO_2/CC cathodes are tested in a full discharge-charge mode at 100 mA g^{-1} and 500 mA g^{-1} in a range of 2-4.3 V **(Figure. S5)**. The discharge capacity of the MnO_2/CC cathode is

reduced to ~250 mA h g^{-1} after merely five cycles at 100 mA g^{-1}. In contrast, for the $Co_{0.2}Mn_{0.8}O_2$/CC cathode, a discharge capacity of 1200 mA h g^{-1} is still maintained at 100 mA g^{-1} after 200 cycles. Both capacity and cycability are remarkably improved by using the Co-doped MnO_2 cathode.

Figure. 2c shows the first discharge-charge voltage profiles of the $Co_{0.2}Mn_{0.8}O_2$/CC cathode at 100, 200 and 500 mA g^{-1} under a limited capacity of 1000 mA h g^{-1}. The overpotential of the $Co_{0.2}Mn_{0.8}O_2$/CC cathode is ~0.73 V, which is about only 58% of that of the pure MnO_2/CC. In addition, the cyclability performance of Li-CO_2 batteries with different cathodes are evaluated at 100, 200 and 500 mA g^{-1} with a limited capacity of 1000 mA h g^{-1} (**Fig. 2d-e** and **Figure. S6**). The overpotential of the $Co_{0.2}Mn_{0.8}O_2$/CC cathode does not increase significantly even after testing 500 cycles, indicating its outstanding cycling stability. Compared with other Co-doped MnO_2 samples **(Figure. 1e**) and the MnO_2/CC cathode (**Figure. S7-8**), the $Co_{0.2}Mn_{0.8}O_2$/CC cathode shows the largest specific capacity and the lowest overpotential (**Figure. S8c**).

The attractive characters of the Li-CO_2 batteries lie in the long-term cyclability together with a low overpotential. The electrochemical performances of the $Co_{0.2}Mn_{0.8}O_2$/CC cathode were compared with those of current catalysts reported so far. As summarized in **Figure. 1f**, the cycling performance of Li-CO_2 batteries with the $Co_{0.2}Mn_{0.8}O_2$/CC cathode is the best among all the Li-CO_2 batteries. Simultaneously, the overpotential of the $Co_{0.2}Mn_{0.8}O_2$/CC cathode is the lowest (~0.73 V), which overwhelms those of other catalysts.[10, 11, 13,14, 15, 22-28]

2.3. Reaction process

Figure. 3a shows the initial galvanostatic discharge-charge curve of the Li-CO_2 battery with the $Co_{0.2}Mn_{0.8}O_2$/CC cathode at the current density of 100 mA g^{-1}. The positions A, B, C and D represent the different stages of the cell. XRD patterns (**Figure. 3b**) reveal that the peaks of Li_2CO_3 are emerged after discharging from the position A to the position C. In contrast, the

peaks of Li_2CO_3 are gradually disappeared after charging from the position C to the position D. The process has further been confirmed by Raman spectra (**Figure. 3c)**, in which the appearance/disappearance of carbonate stretching peaks at 1080 cm^{-1} revealed the formation/decomposition of the Li_2CO_3 . [12] This process is consistent with the reaction product of other Li-CO_2 batteries. [10] The *ex-situ* SEM images (**Figure. 3d-f)** show the morphology variation of the $Co_{0.2}Mn_{0.8}O_2$/CC cathode in Li–CO_2 batteries. After discharging to the position C, cotton-like discharge products are formed on the surface of the $Co_{0.2}Mn_{0.8}O_2$/CC cathode, corresponding to the formation of discharge Li_2CO_3 product. In turn, the smooth nanowires are reappeared when it charges to the position D. Note that the same nanowire morphology and XRD peaks of the $Co_{0.2}Mn_{0.8}O_2$/CC electrode remain even after 50 cycles, suggesting the full decomposition of Li_2CO_3 products (**Figure. S9**). It demonstrates that the CC/$Co_{0.2}Mn_{0.8}O_2$ cathode has a good ability to facilitate the formation/decomposition of Li_2CO_3.

To further elucidate the reaction process of the $Co_{0.2}Mn_{0.8}O_2$/CC cathode, *in-situ* TEM has been adopted to observe the morphology and structure evolution of the $Co_{0.2}Mn_{0.8}O_2$ during the charge-discharge process in the potential range from -3.2 to +4 V. The TEM images (**Figure. 4**, captured from **Movie 1**) show that the nanowire becomes coarser, and continuously swells by applying a negative potential to the $Co_{0.2}Mn_{0.8}O_2$ nanowire against the counter electrode Li. After discharged for 162 s, the diameter increases from 44.3 to 58.1 nm. It is noteworthy that the arrow-shaped morphology in the front of the reaction side reveals that the Li ions diffuse along the surface of the nanowire and react with CO_2 gas. By comparison, when the positive potential is employed on the nanowire, the swell process stopped and started to shrink, and back to 47.2 nm, indicating good reversibility and cycle stability.

In addition, a large number of fine sphere-shaped particles are accumulated on the nanowire surfaces during the discharge process, and the discharge products are gradually eliminated during the charging process. The *in-situ* SAED patterns (**Figure. 4h–j**) show that

the primitive nanowire is composed of MnO_2, and it turns to the composite of MnO_2 and Li_2CO_3 at -3.2 V, and then the nanowire changes to MnO_2 phase at +4 V. It exhibits that the cycle mechanism is related to the presence of Li_2CO_3 product, while the side reactions have been effectively eliminated. These results are also supported by the EELS analysis (**Figure. 4k-l**) and XPS results (**Figure. S10a-c**), in which the appearance/disappearance of only the Li_2CO_3 peaks not only shows no chemical structure change of the $Co_{0.2}Mn_{0.8}O_2$ nanowire during the reaction process, but also it means that the discharge product is hardly residual on the channel walls, promoting the transport of CO_2.

2.4. Catalytic mechanisms

Compared with other catalysts, the new $Co_{0.2}Mn_{0.8}O_2$/CC cathode in the Li-CO_2 batteries offers a low overpotential and long-term cycability. The mains reasons are mainly associated with three aspects: a good conductivity, a larger Brunauer–Emmett–Teller (BET) surface areas and unique Co-doping sites.

Firstly, as shown in **Figure. 5a**, the introduction of Co dopant can improve the conductivity of MnO_2/CC in comparison with that of the primitive MnO_2/CC. Moreover, the conductivity is positive dependent on the Co-doped concentration. Specifically, the conductivity is increasing with increasing Co-doped concentration at the initial stage, and then it reaches a stable value of ~24 S/cm^2. Moreover, the high conductivity is also identified by EIS tests (**Figure. 5b and Figure. S10d**), wherein the lower surface film resistance (R_f) and charge transfer resistance (R_{ct}) (**Table S1-S2**) are achieved in the $Co_{0.2}Mn_{0.8}O_2$/CC cathode compared with the EIS values of the pure alpha-MnO_2. In addition, the overlapped EIS curve after a discharge-charge cycle indicates that the discharge products have been fully decomposed *via* the CO_2 evolution reaction during the charge process.

Secondly, the high rate performance and good cyclability are related to the phase morphology. Differing from the other electrodes, the $Co_{0.2}Mn_{0.8}O_2$/CC cathode not only has a higher conductivity, but also bestows the largest BET surface area (**Figure. 5c-d**). More importantly,

except for the nanoscale pores (3~5 nm), some large pores of 14~30 nm are existing in the $Co_{0.2}Mn_{0.8}O_2$/CC cathode. The high fraction of multiple sized pores is of great importance to accelerate the electrolyte diffusion and the transport of CO_2 gas, resulting in good capacity and rate performance.

Thirdly, to clarify the effect of Co-doped sites on the electrochemical properties of alpha-MnO_2, the Co-doped occupied sites, the density of states (DOS) and the electron local functions (ELF) are calculated by first principles calculations (**Figure. 6**). On the one hand, the positive formation energy of Co-substitution sites (~3.75 eV) reveals that the Co-substitution site is instable. By comparison, the negative formation energies of the three Co-interstitial sites demonstrate that the Co atoms mainly occupy the interstitial sites, specially for the interstitial III site (~-5.17 eV, **Figure. S11**). This trend is consistent with the existance of the maxiumum value of Co-doping concentration. On the other hand, the DOS (**Figure. 6d-f**) mappings show that the pure alpha-MnO_2 is a typical oxide insulator, with a wide Fermi energy. The Co-doping can remarkably reduce the Fermi energy. Especially, the Co-interstitial site (the interstitial III) significantly induce the bandgap of alpha-MnO_2 to form an impurity band, strengthening the conductivity of alpha-MnO_2 by shortening the energy bandgap. Finally, the ELF images (**Figure. 6g-h**) show that the electron pair of Mn obviously increases in the Co-doped MnO_2. It reveals that the valence bond of Mn-O becomes weaker but the ion character of Mn-O becomes stronger, resulting in the increment of conductivity.

3. Conclusions

In summary, a new Co-interstitial alpha-MnO_2 nanowire catalyst has been synthesized by a simple microwave-assisted reaction. The crystal structure and reaction process were clarified by environmental spherical aberration-corrected TEM observations and theoretical calculations. A Li-CO_2 battery using the optimized $Co_{0.2}Mn_{0.8}O_2$/CC cathode electrode offers a super-low overpotential (~0.73 V) and a long-term cyclability (over 500 cycles at a current density of 100 mA g^{-1}), exceeding the values of Li-CO_2 batteries reported so far. Depending

on experimental observations and DFT calculations, it has been confirmed that the outstanding electrochemical properties are mainly associated with the high conductivity, the large BET surface area and unique Co-interstitial doping sites. These results on Li-CO_2 batteries with low cost, high efficiency, high energy density and structural stability, will greatly contribute to tackle greenhouse effect, and will also provide new avenues for designing advanced metal-air batteries.

Supporting Information
Supporting Information is available from the Wiley Online Library or from the author.

Acknowledgments
We greatly acknowledge the financial support from National Key Research and Development Program (2017YFB0702001), National Natural Science Foundation-Outstanding Youth Foundation (51771162), the High-Performance Computing Platform of Hebei University and Graduate Student Innovative Funding Program of Hebei Province (CXZZBS2019053).

Received: ((will be filled in by the editorial staff))
Revised: ((will be filled in by the editorial staff))
Published online: ((will be filled in by the editorial staff))

References

[1] M. Armand, J. M. Tarascon, Nature **2008**, 451 , 652.

[2] M. S. Dresselhaus, I. L. Thomas, Nature **2001**, 414, 332.

[3] P. G. Bruce, S. A. Freunberger, L. J. Hardwick, J.-M. Tarascon, Nature Mater. **2011**, 11, 19.

[4] M. Leskes, N. E. Drewett, L. J. Hardwick, P. G. Bruce, G. R. Goward, C. P. Grey, Angew. Chem. Int. Ed. **2012**, 51, 8560.

[5] X. Li, S. Yang, N. Feng, P. He, H. Zhou, Chinese J. of Catal. **2016**, 37, 1016.

[6] Y. Liu, R. Wang, Y. Lyu, H. Li, L. Chen, Energy Environ. Sci.**2014**, 7, 677.

[7] B. Liu, Y. Sun, L. Liu, J. Chen, B. Yang, S. Xu, X. Yan, Energy Environ. Sci. **2019**, 12, 887.

[8] X. Zhang, Q. Zhang, Z. Zhang, Y. Chen, Z. Xie, J. Wei, Z. Zhou, Chem. Commun. **2015**, 51, 14636.

[9] Y. Qiao, J. Yi, S. Wu, Y. Liu, S. Yang, P. He, H. Zhou, Joule **2017**, 1, 359.

[10] Z. Zhang, Q. Zhang, Y. Chen, J. Bao, X. Zhou, Z. Xie, J. Wei, Z. Zhou, Angew. Chem. Int. Ed. Engl. **2015**, 54, 6550.

[11] Z. Zhang, X. G. Wang, X. Zhang, Z. Xie, Y. N. Chen, L. Ma, Z. Peng, Z. Zhou, Adv Sci, **2018**, 5, 1700567.

[12] L. Qie, Y. Lin, J. W. Connell, J. Xu, L. Dai, Angew. Chem. Int. Ed. **2017**, 56, 6970.

[13] S. Bie, M. Du, W. He, H. Zhang, Z. Yu, J. Liu, M. Liu, W. Yan, L. Zhou, Z. Zou, ACS Appl. Mater. Inter. **2019**, 11, 5146.

[14] S.-M. Xu, Z.-C. Ren, X. Liu, X. Liang, K.-X. Wang, J.-S. Chen, Energy Storage Mater. **2018**, 15, 291.

[15] R. Pipes, A. Bhargav, A. Manthiram, ACS Appl. Mater. Interfaces **2018**, 10, 37119.

[16] W. Ma, S. Lu, X. Lei, X. Liu, Y. Ding, J. Mater. Chem. A **2018**, 6, 20829.

[17] Y. Mao, C. Tang, Z. Tang, J. Xie, Z. Chen, J. Tu, G. Cao, X. Zhao, Energy Storage Mater. **2019**, 18, 405.

[18] B. Ge, Y. Wang, Y. Sun, Y. Li, J. Huang, Q. Peng, Energy Storage Mater. **2019**, DOI: https://doi.org/10.1016/j.ensm.2019.02.018.

[19] D. Banerjee, H. W. Nesbitt, Geochim. Cosmochim. Acta **1999**, 63, 3025.

[20] T. V. Thi, A. K. Rai, J. Gim, J. Kim, J. Power Sources **2015**, 292, 23.

[21] Z. Hu, X. Xiao, C. Chen, T. Li, L. Huang, C. Zhang, J. Su, L. Miao, J. j. Jiang, Y. R. Zhang, J. Zhou, Nano Energy **2015**, 11, 226.

[22] Y. Hou, J. Wang, L. Liu, Y. Liu, S. Chou, D. Shi, Huakun Liu, Y. P. Wu, W. M. Zhang, J. Chen. Adv. Fun. Mater. **2017**, 27,1700564.

[23] S. Yang, Y. Qiao, P. He, Y. Liu, Z. Cheng, J.-j. Zhu, H. Zhou, Energy Environ. Sci. **2017**, 10, 972.

[24] Z. Zhang, Z. Zhang, P. Liu, Y. Xie, K. Cao, Z. Zhou, J. Mater. Chem. A **2018**, 6, 3218.

[25] Z. Guo, J. Li, H. Qi, X. Sun, H. Li, A. G. Tamirat, J. Liu, Y. Wang, L. Wang, Small **2018**, 0, 1803246.

[26] Y. Jin, C. Hu, Q. Dai, Y. Xiao, Y. Lin, J. W. Connell, F. Chen, L. Dai, Adv. Funct. Mater. **2018**, 28, 1804630.

[27] C. Wang, Q. Zhang, X. Zhang, X. G. Wang, Z. Xie, Z. Zhou, Small **2018**, 14, 1800641.

[28] Z. Zhang, C. Yang, S. Wu, A. Wang, L. Zhao, D. Zhai, B. Ren, K. Cao, Z. Zhou, Adv. Energy Mater. **2019**, 9, 1802805.

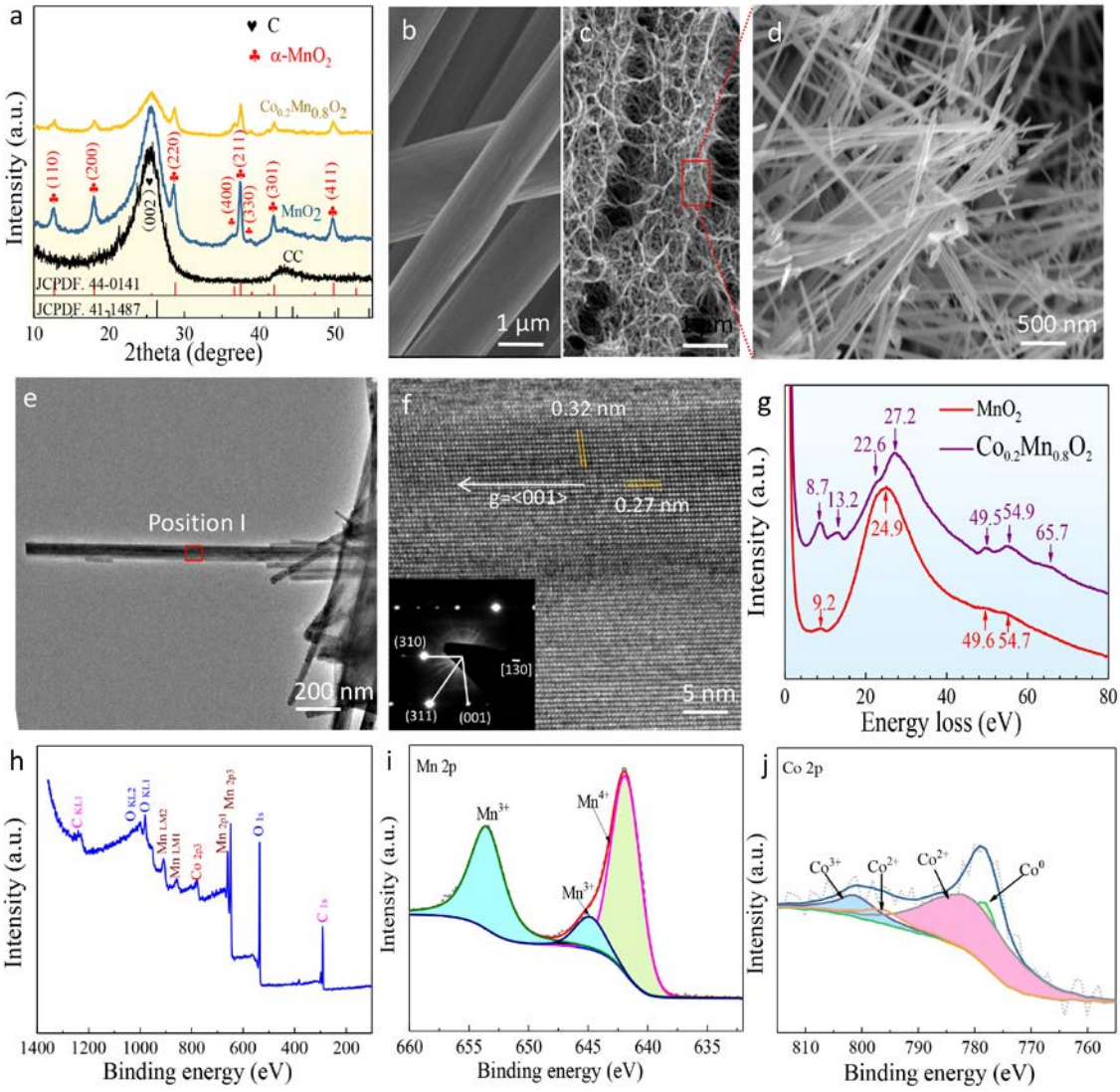

Figure 1. **Microstructural characteristics**. (**a**) XRD patterns of representative the CC, MnO_2/CC and $Co_{0.2}Mn_{0.8}O_2$/ CC. (**b**) SEM image of the CC. (**c**) SEM image of the $Co_{0.2}Mn_{0.8}O_2$/ CC. (**d**) High-magnification SEM image of the $Co_{0.2}Mn_{0.8}O_2$/ CC. (**e**) TEM image of the $Co_{0.2}Mn_{0.8}O_2$/ CC. (**f**) HRTEM image of a $Co_{0.2}Mn_{0.8}O_2$, nanowire, the inside is the SAED pattern of the $Co_{0.2}Mn_{0.8}O_2$ nanowire. (**g**) Low-loss EELS mappings of the MnO_2/CC (red) and the $Co_{0.2}Mn_{0.8}O_2$/CC (purple). (**h**) XPS profile of the $Co_{0.2}Mn_{0.8}O_2$. (**i**) and (**j**) Local high magnification XPS profiles of Mn 2*p* and Co 2*p*, respectively.

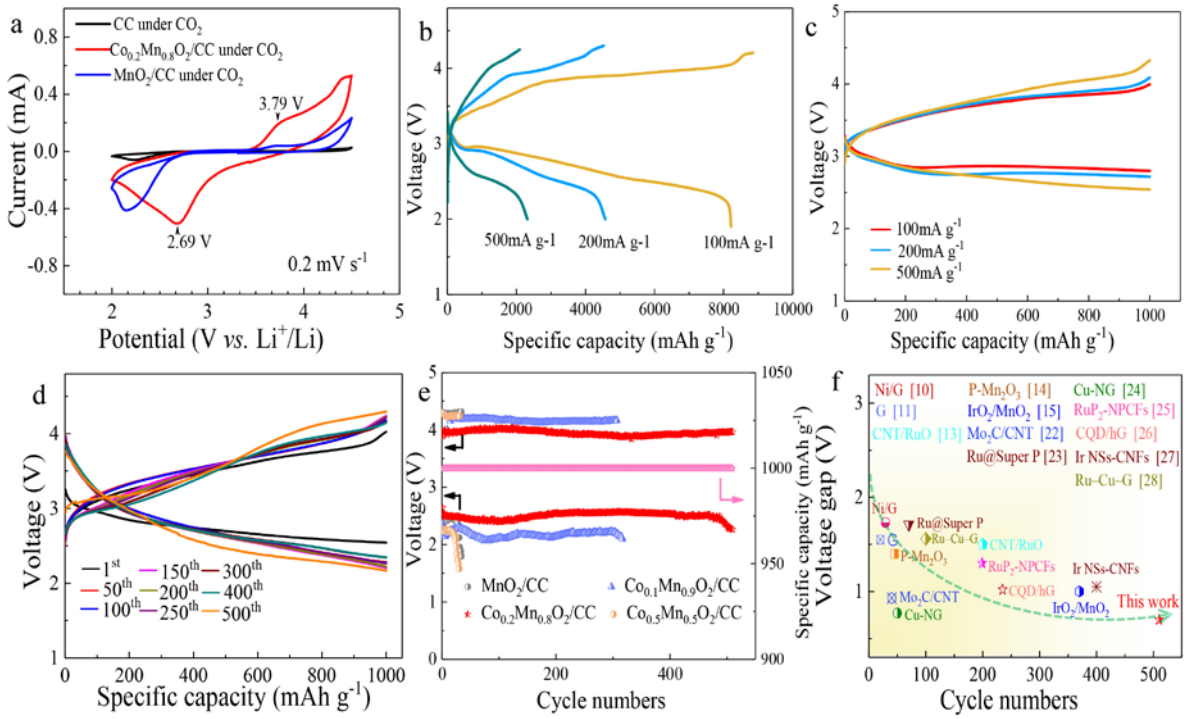

Figure 2. Electrochemical properties of Li-CO_2 batteries. (**a**) CV curves recorded at a scan rate of 0.2 mV s^{-1} over a voltage range of 2-4.5 V *vs.* Li/Li^+ in a CO_2-saturated condition. (**b**) The first charge/discharge properties under different current densities. (**c**) Discharge-charge curves of the $Co_{0.2}Mn_{0.8}O_2$/CC sample under a controlled capacity of 1000 mA h g^{-1} at different current densities. (**d**) Cycle properties of the $Co_{0.2}Mn_{0.8}O_2$/CC sample under a controlled capacity of 1000 mA h g^{-1} at 100 mA g^{-1}. (**e**) Variation of cutoff voltage of the different samples under a controlled capacity of 1000 mAh g^{-1} at 100 mA g^{-1}. (**f**) Comparison of cycle performance and charge/discharge voltage gap for the typical Li-CO_2 batteries reported so far. [10, 11, 13-15, 22-28]

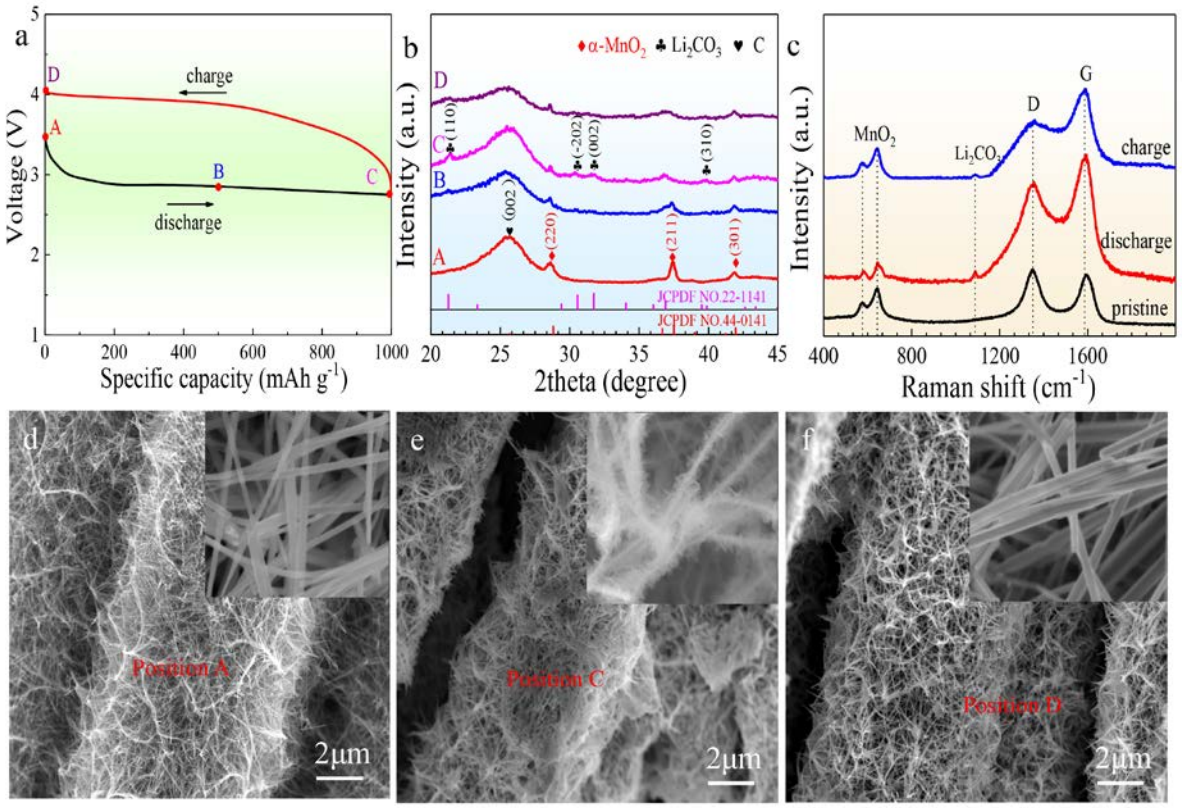

Figure 3. Characteristics of the discharge-discharge products. (**a**) Initial cycle galvanostatic discharge/charge profiles. (**b**) XRD patterns of the samples corresponding to the different positions in (**a**). (**c**) Raman spectra of the different states. Typical SEM images of $Co_{0.2}Mn_{0.8}O_2$/CC cathodes with the pristine (**d**), the discharged state (**e**) and the charge state (**f**), respectively. The insets are the local high magnification images.

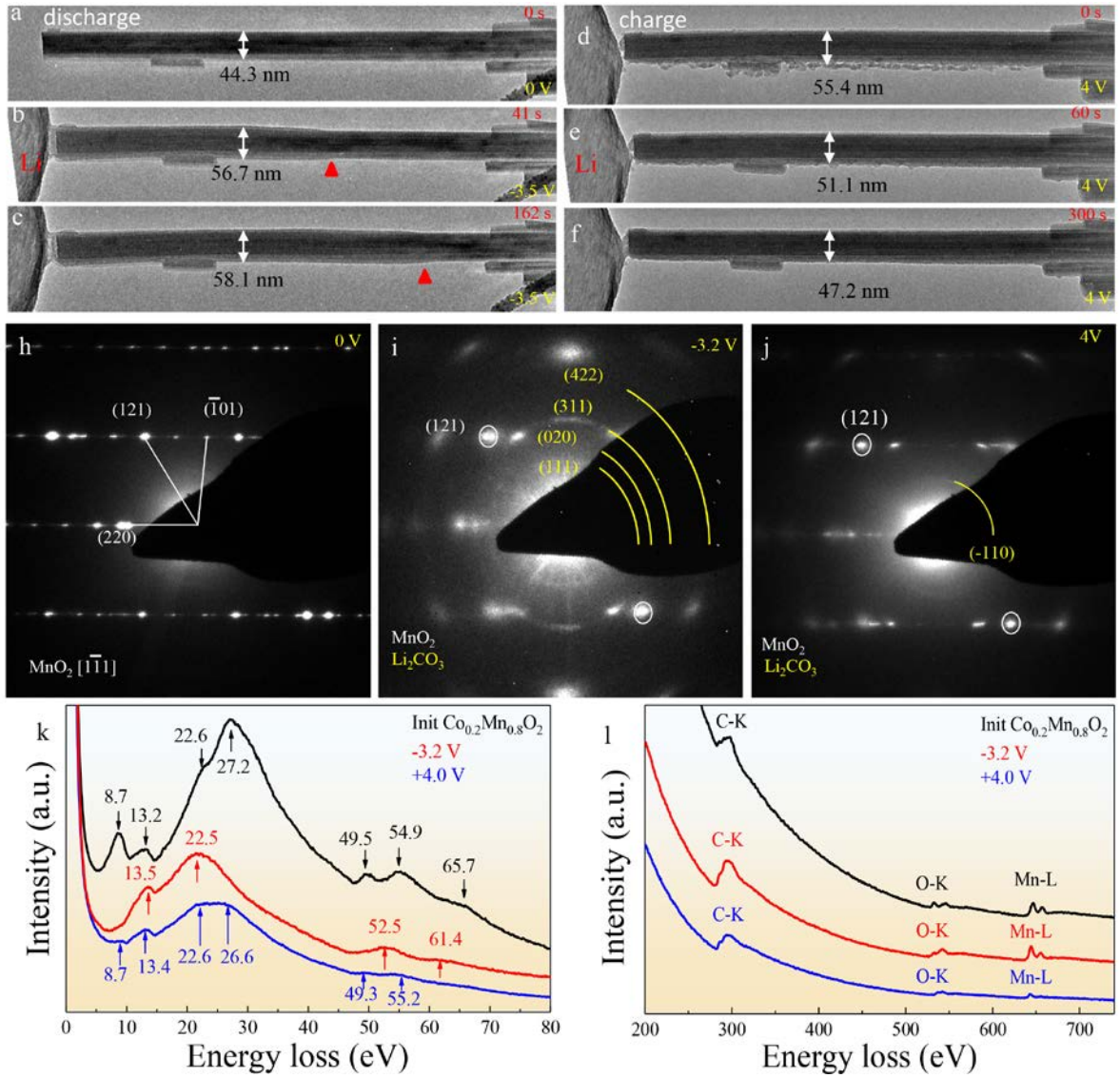

Figure 4. *In-situ* microstructural features of the $Co_{0.2}Mn_{0.8}O_2$/CC electrode. Typical morhpology varaition during the discharge process (**a-c**) and the charge process (**d-f**). *In-situ* SAED patterns of the primitive (**h**), the discharge (**i**) and the charge (**j**) $Co_{0.2}Mn_{0.8}O_2$ nanowires. (**k**) and (**l**) Low-loss and core-loss EELS mappings of the $Co_{0.2}Mn_{0.8}O_2$/CC electrode at different states.

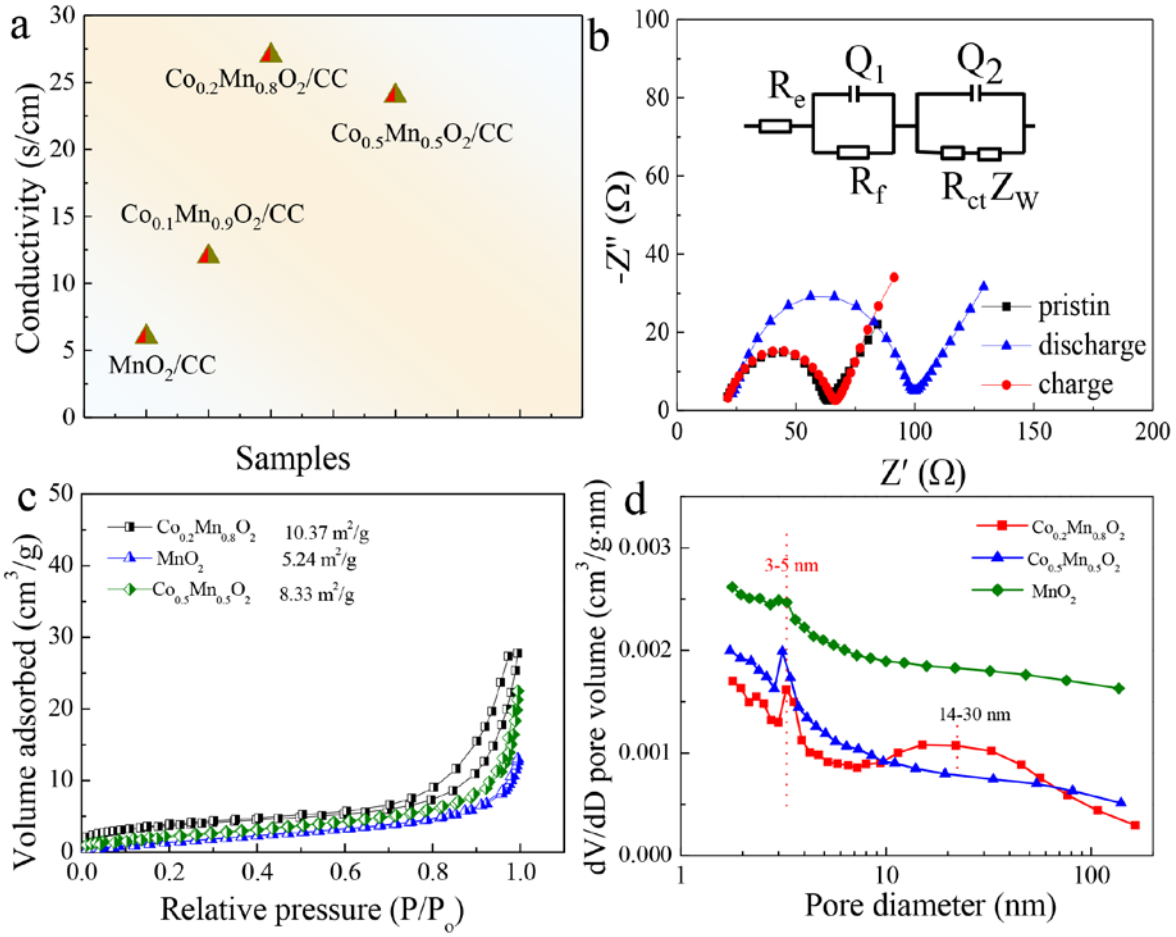

Figure 5. Mechanisms for outstadning electrochemical properties. (**a**) The conductivity values of the different MnO_2-based electrodes. (**b**) EIS spectra of the **$Co_{0.2}Mn_{0.8}O_2$/CC** eletrodes under different conditions. The inset corresponds to the fitting circuit. (**c**) The nitrogen adsorption-desorption isotherms of different samples. (**d**) The pore size distribution of different samples.

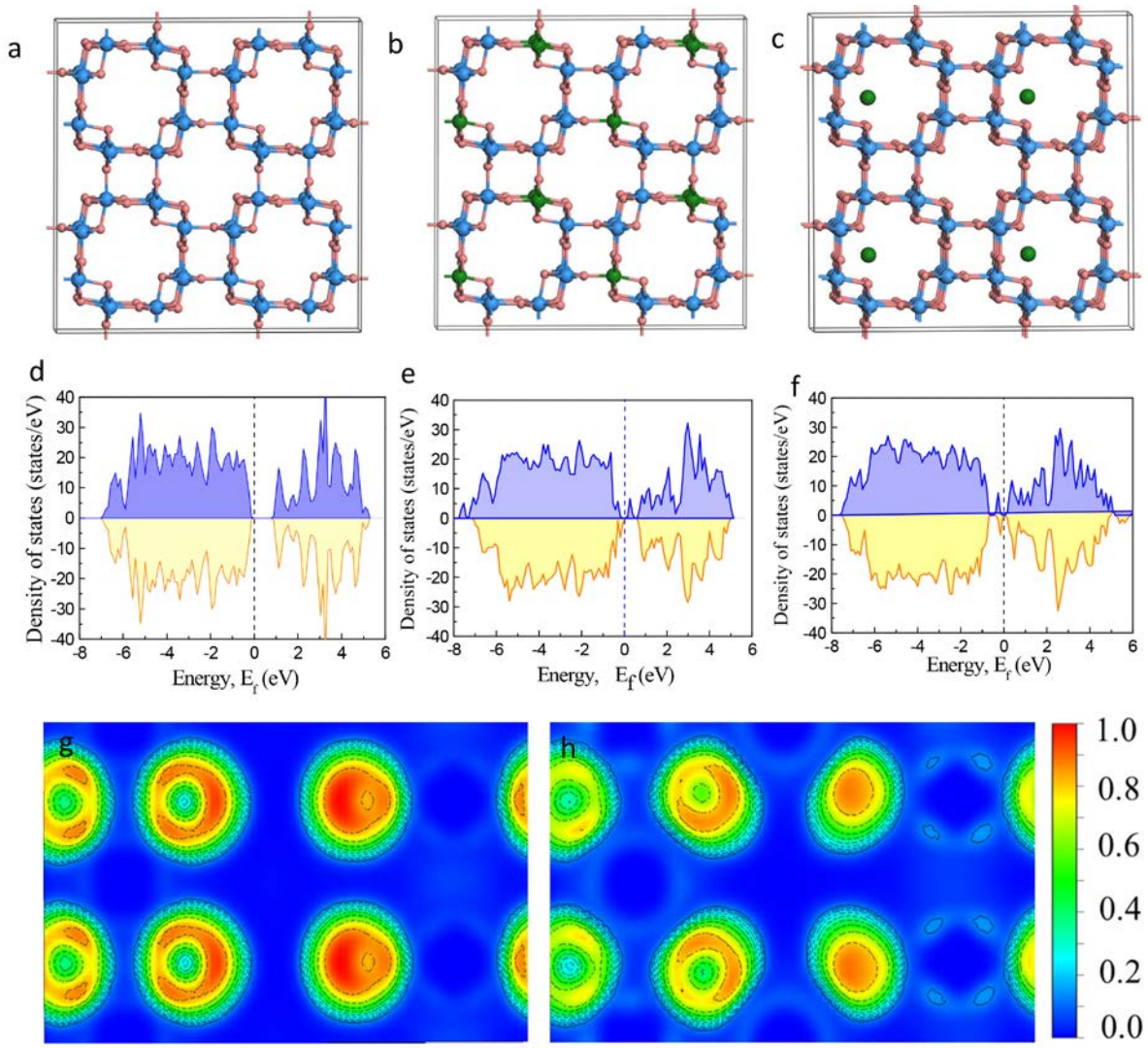

Figure 6. Theoritical interpretation. Optimized atomic structures: (**a**) the pristine α-MnO_2, (**b**) the Co-substitutional alpha-MnO_2, and (**c**) the Co-doped alpha-MnO_2 (the interstitial-III site). The wathet blue, green and pink balls stand for Mn, Co and O atoms, respectively. Density of states: (**d**) the pristine alpha-MnO_2, (**e**) the Co-substitutional alpha-MnO_2 , and (**c**) the Co-doped alpha-MnO_2 (the interstitial-III site). ELF images: (**g**) the pristine alpha-MnO_2 and (**h**) the Co-doped alpha-MnO_2 (the interstitial-III site).

We prepare a new Co-doped alpha-MnO_2 nanofiber catalyst for Li-CO_2 batteries, and it shows a large capacity of 8160 mA h g^{-1}, a low overpotential of 0.73 V and an ultrahigh cyclability (500 cycles), by improving the conductivity, enhancing the catalytic activity and prohibiting side reactions. The catalyst is highlighted by its simplicity and high-yield production of a well-defined morphology, which attributes to the industrial development of Li-CO_2 batteries.

Keyword: Catalytic Cathodes

Bingcheng Ge, Yong Sun, Jianxin Guo, Carlos Fernandez, Qiuming Peng*

A Co-Doped MnO_2 Catalyst for Li-CO_2 Batteries with Low Overpotential and Ultrahigh Cyclability

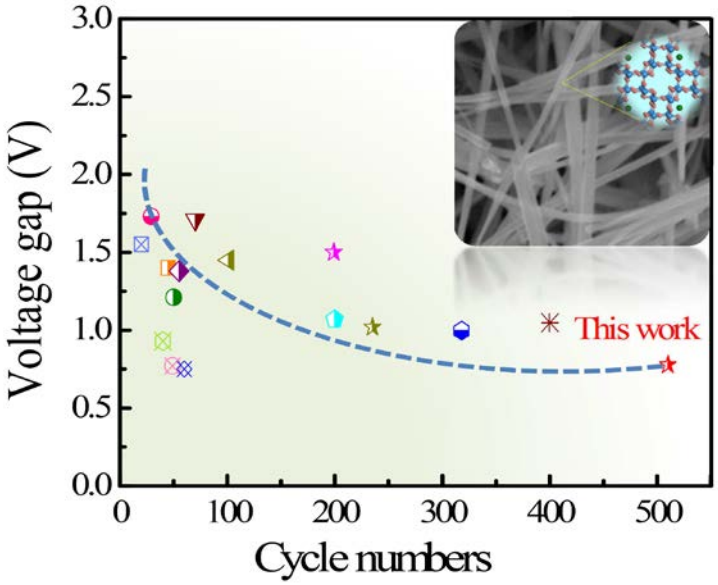

Supporting Information

A Co-Doped MnO_2 Catalyst for Li-CO_2 Batteries with Low Overpotential and Ultrahigh Cyclability

*Bingcheng Ge, Yong Sun, Jianxin Guo, Xiaobin Yan, Carlos Fernandez, and Qiuming Peng**

Supporting Information

A Co-Doped MnO_2 Catalyst for Li-CO_2 Batteries with Low Overpotential and Ultrahigh Cyclability

Bingcheng Ge, Yong Sun, Jianxin Guo, Xiaobin Yan, Carlos Fernandez, Qiuming Peng[*]

Experimental sections

Preparation of $Co_xMn_{1-x}O_2$/CC electrodes

All the reagents obtained from Aladdin (shanghai, china) were of analytical grade and used without any further purification. The Co-doped alpha-MnO_2 nanowires were prepared by a microwave-assisted method. A microwave system (MS, XH-8000, Beijing XiangHu Science and Technology Development Co., Ltd., China) equipped with *in situ* magnetic stirring was used to heat the autoclave. $MnSO_4 \cdot H_2O$ (0.029 g), $KMnO_4$ (0.335g) and $Co(NO_3)_2 \cdot 6H_2O$ were dissolve into 20 mL of deionized water, respectively. Different molar ratios of $Co(NO_3)_2 \cdot 6H_2O$: $MnSO_4 \cdot H_2O$ were used as Co-dopant reagents. After stirring for about 30 minutes at room temperature, a piece of CC (5×5 cm^2) was immersed in the mixed solution and heated to 140 °C at a heating rate of 10 °C/min, and kept for 60 min with a power of 600 W. After the microwave reaction, the CC which covered with Co-doped MnO_2 nanowires was rinsed with deionized water. All unreacted materials were removed, and the obtained samples were dried under a vacuum at 80 ^oC for 24 h. The different Co^{2+}: Mn^{2+} molar ratios of 0:1, 0.1:0.9, 0.2:0.8 and 0.5:0.5 in the initial solutions were performed, and the products were designated as MnO_2, $Co_{0.1}Mn_{0.9}O_2$, $Co_{0.2}Mn_{0.8}O_2$ and $Co_{0.5}Mn_{0.5}O_2$, respectively.

Material characterization

XRD patterns were collected on a Rigaku D/Max- 2500 diffractometer using a filtered Cu Kα radiation at a sweep rate of 4 degree/min, SEM was conducted with a Hitachi S-4800. TEM images and EELS analysis were observed on a Titan ETEM G2 at 300 kV. A H7756 four-point probe was used to determine the electrical conductivity of the obtained samples. The surface areas and pore size distribution were performed on a micrometrics ASAP2020 analyzer at 196 C. XPS was conducted on a ThermoFisher with Al Kα (1486.71 eV) X-ray radiation (15 kV and 10 mA). The binding energies obtained in the XPS analysis were corrected by referencing the C 1*s* peak position (284.40 eV).

Li-CO_2 battery assembly

The Li-CO_2 battery assembly was based on a CR2032 coin type battery. It was successively assembled by stacking a lithium metal anode (14 mm in diameter), a piece of glass fiber separator (16 mm in diameter) soaked with 80 μL of electrolyte, and a cathode placed on a nickel foam supporter. The $Co_xMn_{1-x}O_2$/CC cathodes were cut into disks. A hole (4 mm in diameter) was drilled in the cathode shell so that the CO_2 can easily and quickly accesses the cathode. Then, the assembled batteries were placed in a 250 mL glass vessel filled with high-purity CO_2. The pure CO_2 was pumped into the glass vessel through the straight two-way piston conducted alternatively by vacuuming and ventilating three times. After incubating for 10 h, the discharge and charge cycle of the batteries were tested. 1 M LiTFSI dissolved in TEGDME solution was chosen as the electrolyte for all Li-CO_2 batteries. All potentials were referenced against Li/Li^+.

Electrochemical test

The galvanostatic discharge/charge tests were collected on a LAND CT2001A battery test instrument. The specific capacity and current density were calculated according to the mass of $Co_xMn_{1-x}O_2$ nanowires on the electrodes. The mass loading of $Co_xMn_{1-x}O_2$ on CC was found to be 0.5-0.8 mg cm^{-2}. CVs were conducted on a BioLogic VMP3 electrochemical workstation in the potential window of 2.0-4.5 V (*vs.* Li/Li^+), and the scan rate was 0.2 mV s^{-1}. EIS curves were carried out on a BioLogic VMP3 system with the typical frequency range from 100 kHz to 10 mHz by applying the applied voltage of 5 mV.

First-principles calculations

The calculations were finished with the Vienna ab initio Simulation Package (VASP) code in terms of DFT. The function and approximation have been introduced in previous results [S1]. The core electrons are represented by the projected enhanced wave potential. The kinetic energy cutoff above 500 eV and the K point sampling on the unit cell are 3×3×4 for 2×2×2 supercell of pristine and doping alpha-MnO_2. Structural optimization was performed with a force convergence criterion of 0.01 eV/A. Because Mn is a magnetic atom, the

GGA+U method is employed with U−J = 4 eV, 3 eV for Mn and Co, respectively. The lowest energy magnetic state is set based on antiferromagnetic. The optimized lattice constant of alpha-MnO_2 is a = b = 0.98 nm, c = 0.29 nm.

The formation energy of Co is defined as following [S2]:

(1)

(2)

where and are the formation energies of Co interstitial and substitution, respectively. and E are the corresponding total energies of Co interstitial and substitution, respectively. , E_{Co}, and E_{Mn} are the total energies of alpha-MnO_2, Co and Mn atoms, respectively.

S1. Peng, Q. et al. In-situ atomic-scale phase transformation of Mg under hydrogen conditions. *J. Phys. Chem. C* **122**, 19532-19539 (2018).

S2. Kuwabara, A. & Tanaka, I. First principles calculations of defect formation energies in Sr- and Mg-doped $LaGaO_3$. *J. Phys. Chem. B* **108**, 9168-9172 (2004).

Table S1. Elemental compositions of different samples dependent on EDS analysis

Samples	Elemental composition (at.%)			
	Mn	Co	O	C
MnO_2	14.85	-	47.22	37.93
$Co_{0.1}Mn_{0.9}O_2$	13.90	0.55	44.52	41.03
$Co_{0.2}Mn_{0.8}O_2$	19.28	1.12	41.95	37.65
$Co_{0.5}Mn_{0.5}O_2$	16.95	1.18	41.46	39.54

Table S2. Fitting parameters of EIS curves of the $Co_{0.2}Mn_{0.8}O_2$ sample in terms of fitting circuits.

Sample	$R_e(\Omega)$	R_f (Ω)	Q_1		R_{ct} (Ω)	Q_2	
			Y	n		Y	n
Pristine	19.72	46.05	1.2×10^{-5}	0.71	40.86	3.7×10^{-2}	0.61
1st charge	19.24	31.73	1.8×10^{-4}	0.82	41.37	2.7×10^{-2}	0.59
1st discharge	21.02	73.72	5.1×10^{-5}	0.83	127.19	1.9×10^{-2}	0.77

Table S3. Fitting parameters of EIS curves of the MnO_2 sample in terms of fitting circuits.

Sample	$R_e(\Omega)$	$R_f(\Omega)$	Q_1		$R_{ct}(\Omega)$	Q_2	
			Y	n		Y	n
Pristine	25.61	62.44	2.1×10^{-3}	0.83	185.12	1.6×10^{-5}	0.89
1^{st} charge	38.42	71.16	1.1×10^{-2}	0.85	241.15	7.2×10^{-6}	0.84
1^{st} discharge	25.74	598.51	1.8×10^{-3}	0.82	412.34	4.9×10^{-6}	0.85

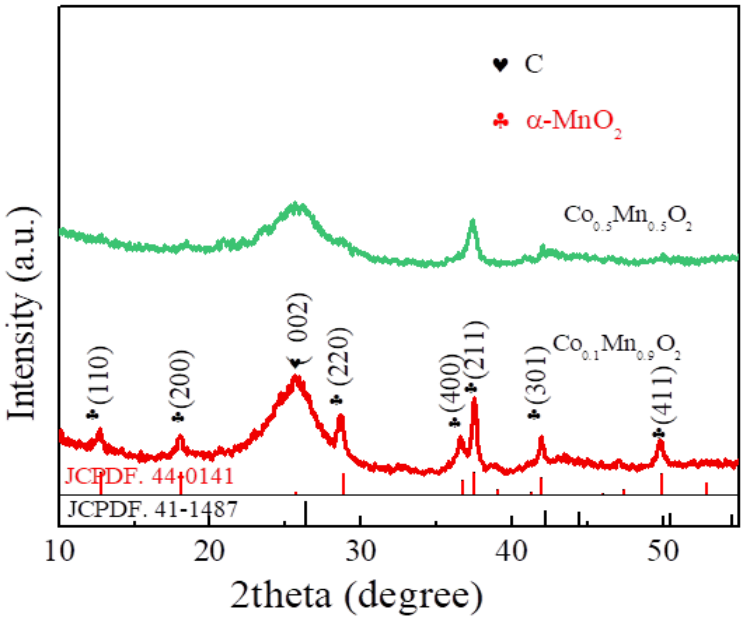

Figure S1. Typical XRD patterns of the different MnO_2 samples

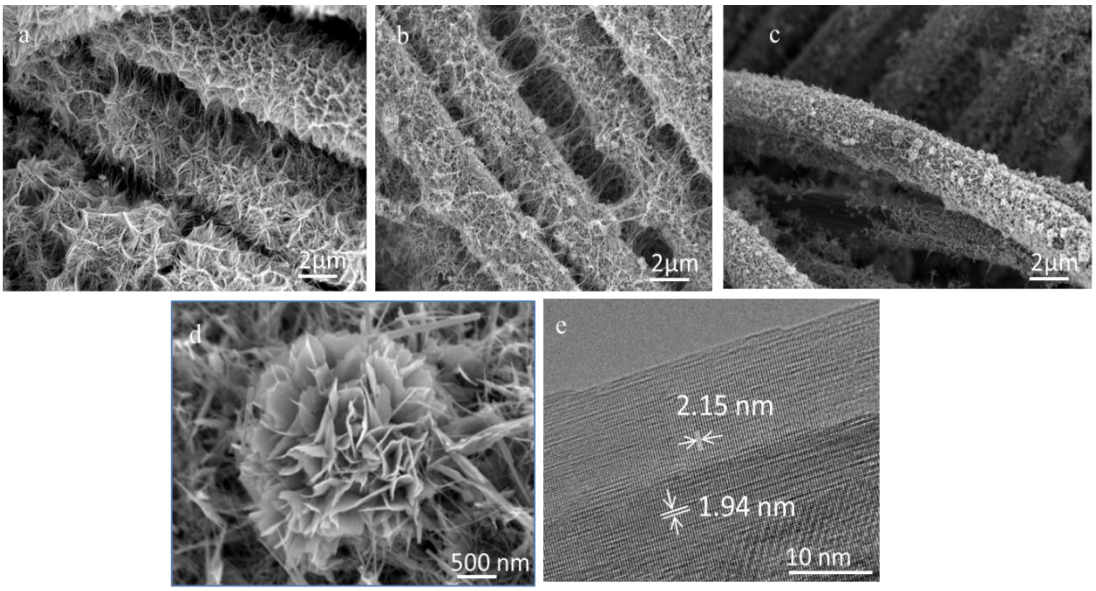

Figure S2. SEM images of the MnO_2 (a), $Co_{0.1}Mn_{0.9}O_2$ (b), $Co_{0.5}Mn_{0.5}O_2$(c). (d) Local high magnification image of plate-shaped $Co_{0.5}Mn_{0.5}O_2$. (e) High revolution TEM image of the plate-like alpha-MnO_2.

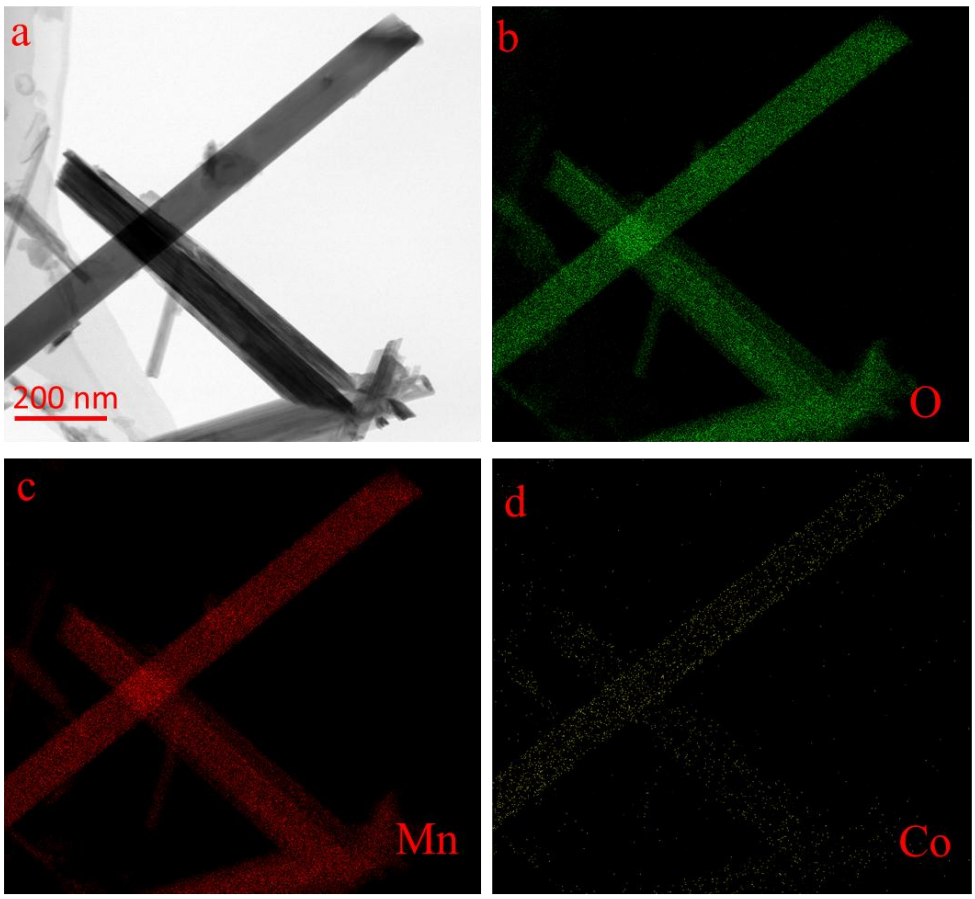

Figure S3. EDS mapping images of Co, Mn and O elements in the $Co_{0.2}Mn_{0.8}O_2$ sample.

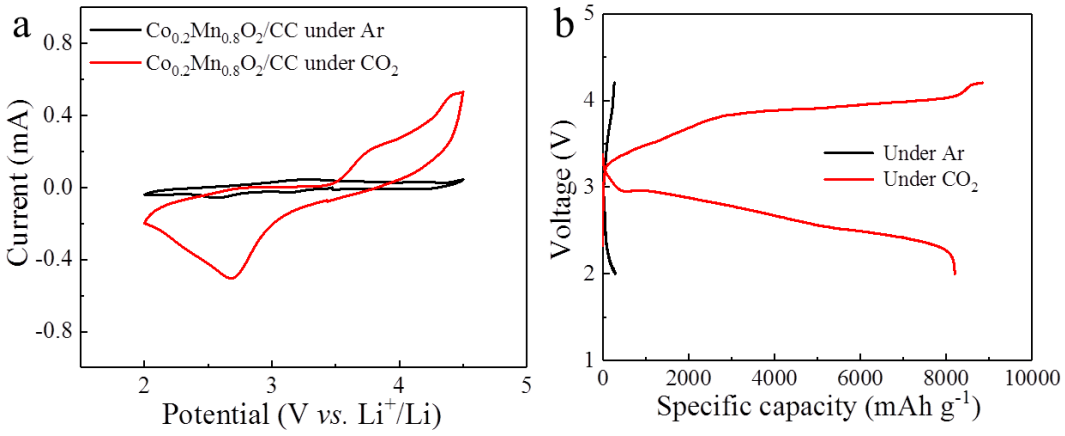

Figure S4. Galvanostatic discharge profiles of the Li-CO_2 cells with pristine $Co_{0.2}Mn_{0.8}O_2$/CC cathode at a current density of 100 mA g^{-1} under both CO_2 and Ar.

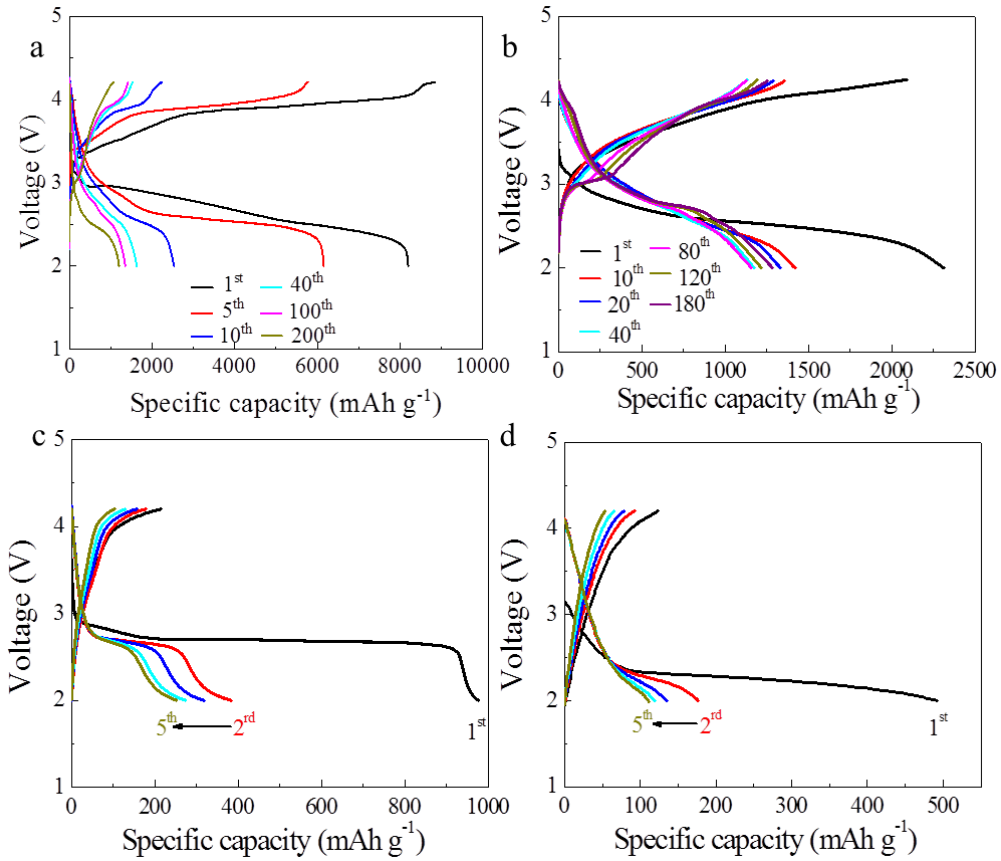

Figure S5. Cycle properties of the $Co_{0.2}Mn_{0.8}O_2$/CC sample under a controlled current of 100 mA g^{-1} (a) and 500 mA g^{-1} (b), respectively. Cycle properties of the pure MnO_2/CC sample under a controlled current of 100 mA g^{-1}(c) and 500 mA g^{-1}(d).

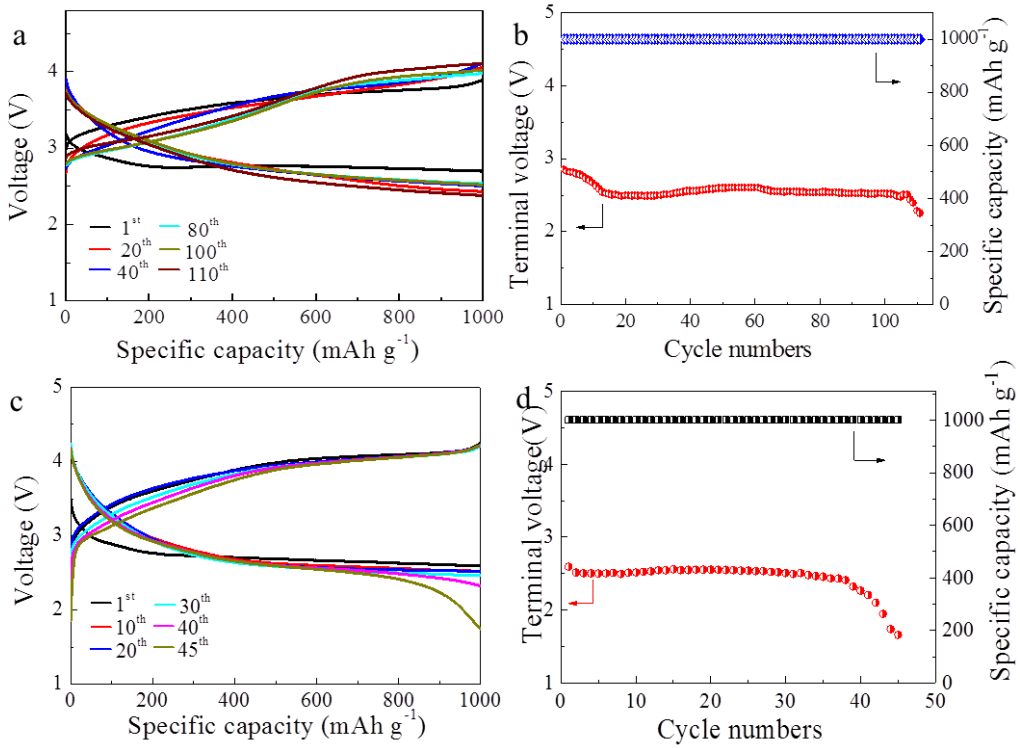

Figure S6. Cycle performance and variation of cutoff voltage of Li-CO_2 batteries with the $Co_{0.2}Mn_{0.8}O_2$/CC electrodes with a controlled specific capacity of 1000 mAh g^{-1} at 200 mA g^{-1} (*a* and b) and 500 mA g^{-1} (c and d).

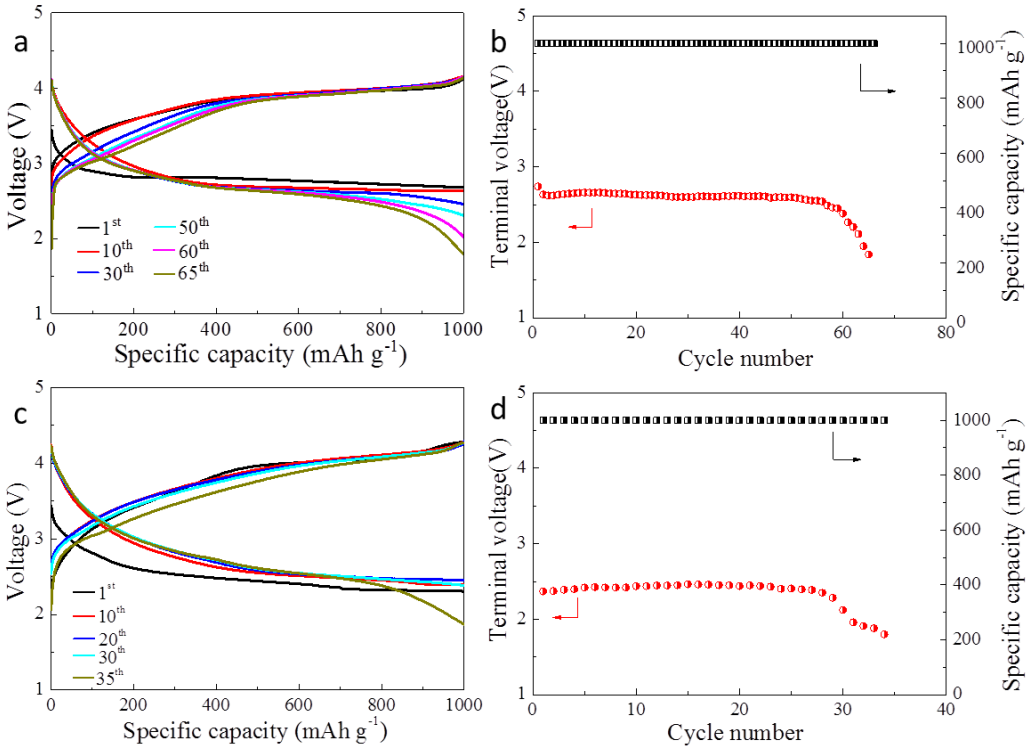

Figure S7. Cycle performance and variation of cutoff voltage of Li-CO_2 batteries with the MnO_2/CC electrodes with a controlled specific capacity of 1000 mAh g^{-1} at 200 mA g^{-1} (a and b) and 500 mA g^{-1} (c and d).

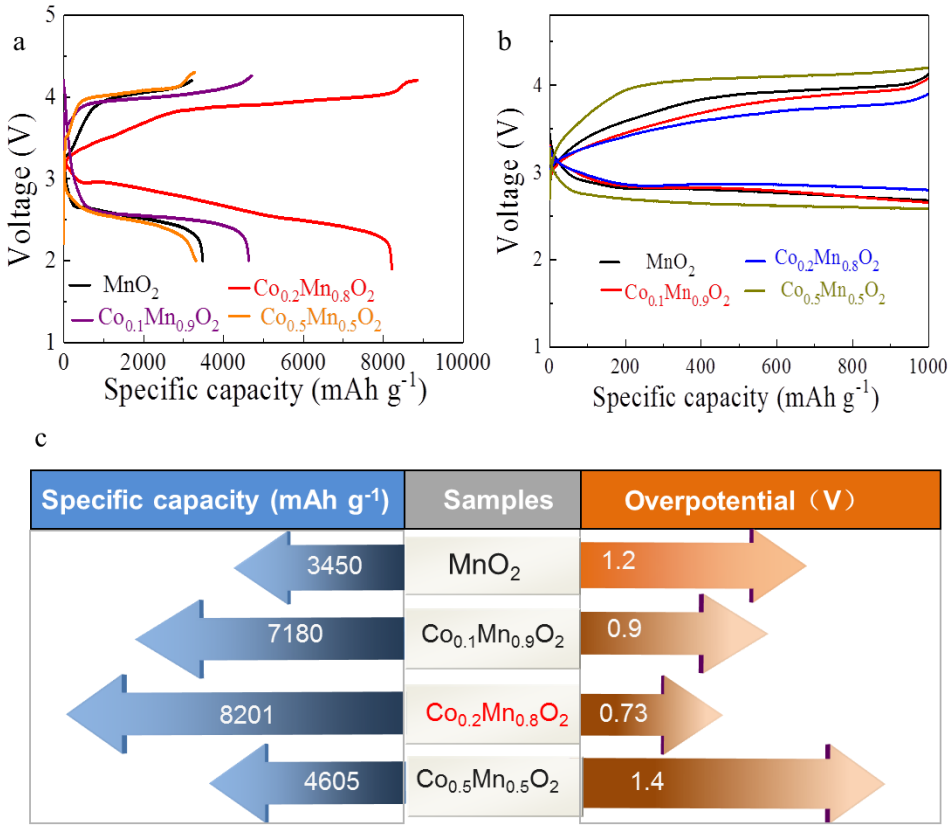

Figure S8. (a) The comparison of charge/discharge capacities of different samples under the same current density of 100 mA g^{-1}. (b) The first charge/discharge curve of different samples under a controlled capacity of 1000 mA h g^{-1} at 100 mA g^{-1}. (c) The comparison of capacity and overpotential of different samples at the same current density of 100 mA g^{-1}.

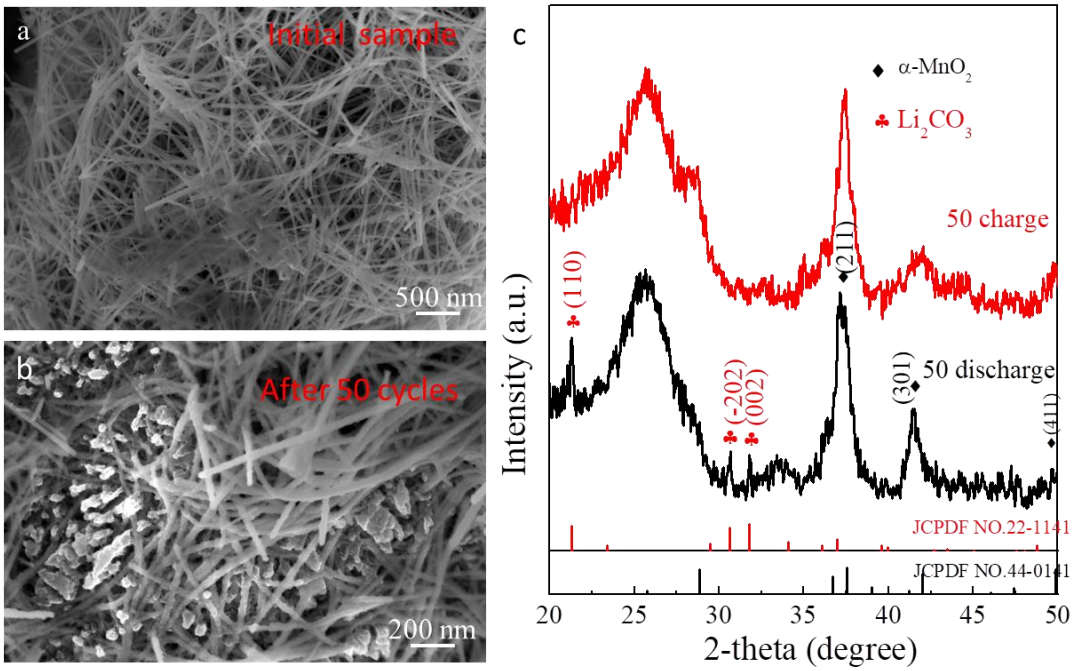

Figure S9. (a) SEM image of the initial $Co_{0.2}Mn_{0.8}O_2$ /CC. (**b**) SEM image of the $Co_{0.2}Mn_{0.8}O_2$ /CC the after 50 cycles. (**c**) XRD patterns of the different state samples.

.

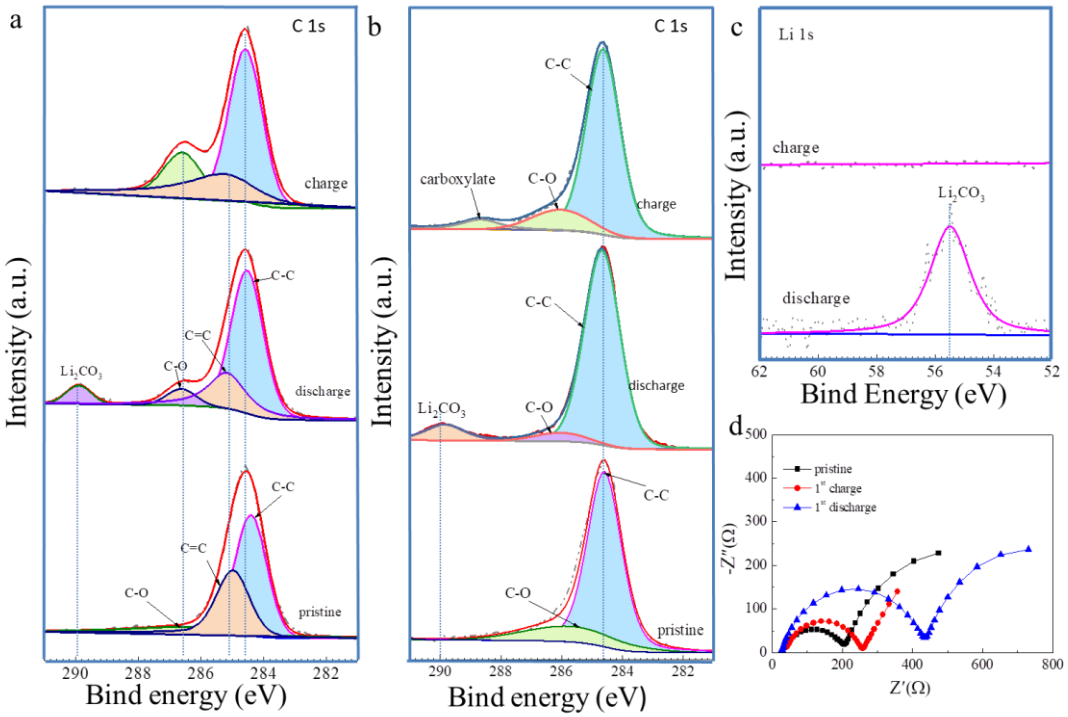

Figure S10. C1*s* XPS profiles of the $Co_{0.2}Mn_{0.8}O_2$/CC eletrode (**a**) and the MnO_2/CC electrode (**b**) under the different states. (**c**) Li 1*s* XPS profile of the $Co_{0.2}Mn_{0.8}O_2$/CC electrode. (**d**) EIS spectra of the bare MnO_2 catalyst for Li-CO_2 batteries under different conditions.

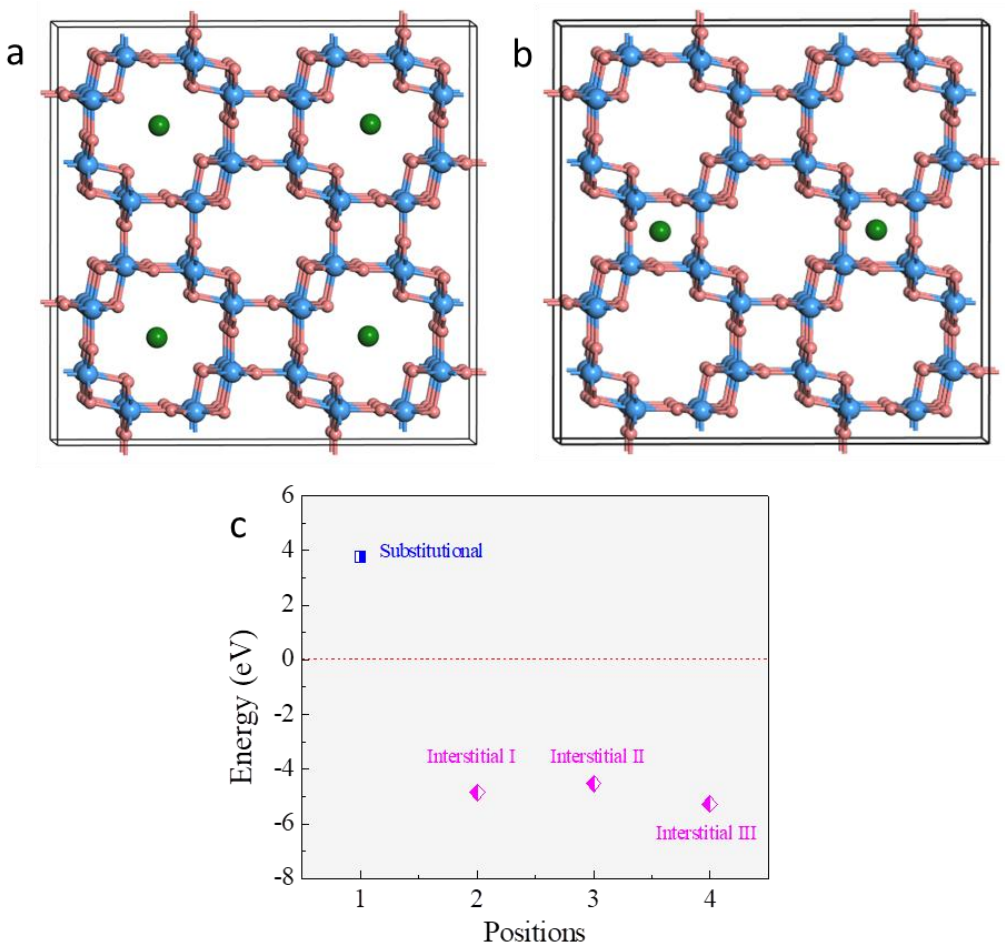

Figure S11. Two occupied sites of the Co-interstitial alpha-MnO_2, (a) the interstitial I, (b) the interstitial II. (c) The formation energies of different occupied sites.